Chapter 2

Standard Model and Neutrino Production at LEP

This chapter begins with an overview of the Standard Model of electroweak interactions, concentrating on the areas relevant to the analyses in this thesis. I then describe the production of the single- and multi-photon events with missing energy in e^+e^- collisions via initial-state radiation in the neutrino pair-production process. In Chapter 3, I will also discuss several new physics models whose manifestations can be found using this event signature at the LEP e^+e^- collider.

2.1 The Standard Model

2.1.1 Introduction

The goal of particle physics is to describe the elementary constituents of matter and the interactions among them. This field of physics entered its modern phase at the end of the nineteenth century following a number of fundamental discoveries, including the discovery of the electron, the first particle still considered elementary today, by J.J. Thomson in 1897 [1].

Over the next 70 years our understanding of the particle world advanced by leaps and bounds, culminating in the development of the Standard Model of particle physics. The electroweak theory, developed by S. L. Glashow, A. Salam, and S. Weinberg from 1961 to 1968 provides a unified description of electromagnetic and weak interactions [2]. The problem of mass generation in the gauge theories was illuminated by P.W. Higgs in 1964 [3]. The theory of quantum chromodynamics

Fermions						
Family	Lepton	Electric charge	Mass (MeV)	Quark	Electric charge	Mass (GeV)
1.	ν_e	0	$< 3 \cdot 10^{-6}$	u	2/3	$(1.5 - 4) \times 10^{-3}$
	e	–1	0.511	d	–1/3	$(4 - 8) \times 10^{-3}$
2.	ν_μ	0	< 0.19	c	2/3	1.15 – 1.35
	μ	–1	105.7	s	–1/3	0.08 – 0.13
3.	ν_τ	0	< 18.2	t	2/3	174.3 ± 5.1
	τ	–1	1777	b	–1/3	4.1 – 4.4

Gauge bosons				
Interaction	Symbol	Electric charge	Spin	Mass (GeV)
Electromagnetic	γ	0	1	0
Weak	W	$\pm$ 1	1	80.43 ± 0.04
	Z	0	1	91.188 ± 0.002
Strong	g	0	1	0
Gravity	G	0	2	0

Table 2.1: Fundamental constituents of the Standard Model. Particle masses or mass limits are taken from [6]. Graviton, believed to be the carrier of gravity, is also listed.

describing the strong interaction was introduced in 1973 by H. Fritzsch, M. Gell-Mann, H. Leytwyler, D.J. Gross, and F. Wilczek [4]. The proof of renormalizability of the Standard Model was given by G. 't Hooft in 1971 [5]. These theoretical developments comprise the foundations of the Standard Model as a non-Abelian gauge theory based on the symmetry group $SU(3)_C \times SU(2)_L \times U(1)_Y$, where the $SU(3)_C$ group corresponds to the strong interactions of quantum chromodynamics (QCD) and the $SU(2)_L \times U(1)_Y$ groups correspond to the electroweak interactions.

The fundamental particles of Standard Model are divided into fermions and bosons. The fermions are spin 1/2 particles constituting the matter fields. Every fermion has a matching anti-particle with identical mass and opposite quantum numbers. The

fermions can be subdivided into two groups, those that can interact via the strong force, and those that cannot. The first group is called the quarks and the second the leptons. Both groups contain six particles that can be separated into 3 generations (families), each consisting of two leptons or two quarks. The primary leptons of the three generations are electron, muon, and tau; each has an associated neutrino. The quarks are up, down, charm, strange, top, and bottom. Table 2.1 contains a list of the fermions and their masses. It should be noted that the Standard Model contains no explanation for these 3 generations nor the different masses of the fermions.

The bosons are integral spin particles which mediate the interactions between the fermions. The boson sector of the Standard Model includes the photon, the W and Z bosons, the Higgs, and the gluons (see Table 2.1). The photon mediates the electromagnetic force, the W and Z mediate the weak force, and the gluons mediate the strong force. Gravity is not included in the Standard Model, but it is believed to be mediated by spin-2 graviton. The photons and gluons are presumed to be massless, while the W, Z, and Higgs bosons are massive. The mechanism by which the W and Z bosons acquire masses will be discussed in the next section.

The Standard Model theory has so far stood up to all tests that have been applied to it using particle collisions at the highest possible energies reachable today, as well as precision measurements at lower energies. The intermediate heavy vector bosons, W and Z, were discovered in 1983 and 1984 by the CERN SPS experiments UA1 and UA2, with masses in agreement with the expectations of the Standard Model. The third family of fermions has been completed in 1994 and 2000 with the discovery of the top quark and the tau neutrino by the CDF, DØ [7], and DONuT [8] experiments at Fermilab. Figure 2.1 illustrates the success of the Standard Model in describing various fermion and boson production processes in e^+e^- collisions at LEP. It is, however, widely believed that the Standard Model is not a complete theory and is only a low-energy approximation of a more comprehensive theory which should also incorporate gravity. The status of the Standard Model is discussed in more detail in Section 2.1.3.

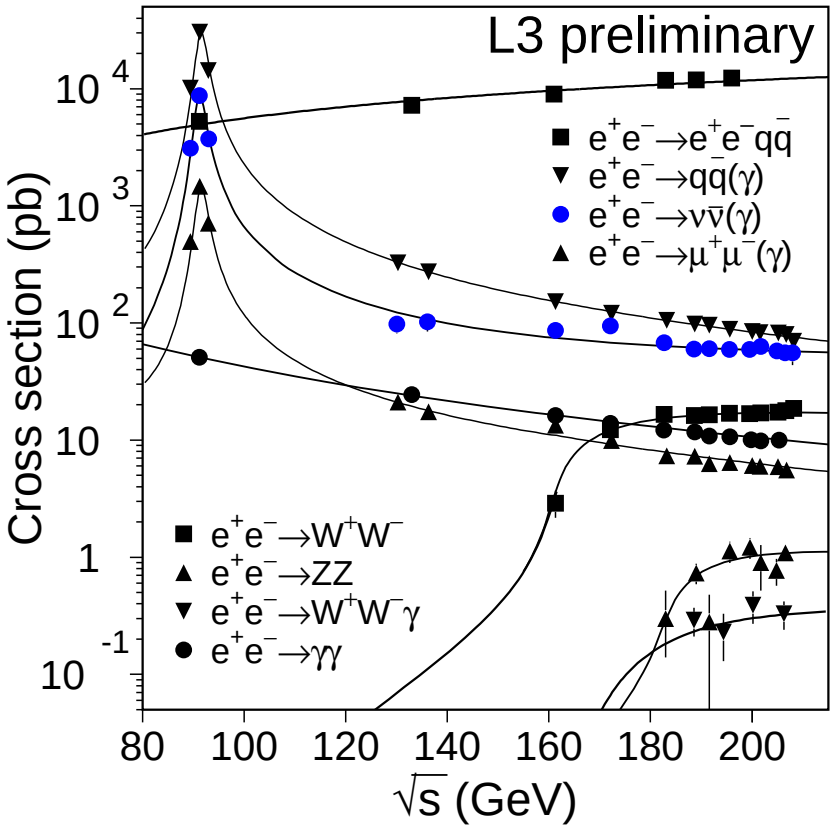

Figure 2.1: Standard Model at LEP: the curves show the Standard Model predictions for the cross-sections of various production processes expected to be observed in e^+e^- collisions at center-of-mass energies ($\sqrt{s}$) ranging from 89 GeV to 208 GeV, while the dots represent the actual measurements performed with the L3 detector at LEP [9].

2.1.2 Electroweak Interactions

This thesis concentrates on the electroweak sector of the Standard Model [2], whose Lagrangian can be written as a sum of four terms:

$$\mathcal{L} = \mathcal{L}_{\text{Fermion}} + \mathcal{L}_{\text{Yang-Mills}} + \mathcal{L}_{\text{Higgs}} + \mathcal{L}_{\text{Yukawa}} \,. \tag{2.1}$$

The Fermion Lagrangian describes the dynamics of the fermions, i.e., their kinetic energy and interactions with the gauge bosons. The Yang-Mills Lagrangian contains the kinetic-energy and self-interaction terms of the gauge fields. The Higgs and Yukawa Lagrangians generate the masses of the gauge bosons and fermions, respectively.

Massless Yang-Mills Theory

The construction of the Standard Model electroweak theory starts with an introduction of a gauge-covariant derivative $\mathcal{D}_\mu$ to ensure the gauge invariance of the Lagrangian:

$$\mathcal{D}_\mu = \partial_\mu + i\,g'^2\,\frac{1}{2}\,B_\mu \cdot Y + i\,g\,\vec{W}_\mu \cdot \vec{T}\,, \tag{2.2}$$

where Y and B are the hypercharge and the corresponding gauge field of the $U(1)_Y$ group, $\vec{T}$ denotes the generators of $SU(2)_L$ group (commonly represented by Pauli matrices), the vector-boson triplet $\vec{W}$ is the $SU(2)_L$ gauge field, and g' and g are the $U(1)_Y$ and $SU(2)_L$ couplings, respectively.

The underlying symmetry is spontaneously broken by introducing a complex Higgs doublet (see the next section), and the physical gauge bosons are obtained through mixing of the neutral B and W^3 gauge fields:

$$\begin{aligned} A &= \sin\theta_{\rm W}\,W^3 + \cos\theta_{\rm W}\,B\,, \\ Z &= \cos\theta_{\rm W}\,W^3 - \sin\theta_{\rm W}\,B\,, \end{aligned} \tag{2.3}$$

where A represents the photon, the carrier of the electromagnetic force, and the Z boson carries the neutral weak current; the weak mixing angle is defined as $\cos\theta_W = g/\sqrt{g'^2+g^2}$. The charged weak interactions are mediated by the W^+ and W^- bosons, which are defined as

$$W^\pm \;=\; \frac{1}{\sqrt{2}}\left(W^1 \mp iW^2\right). \tag{2.4}$$

Although the physical vacuum does not have the $SU(2)_L \times U(1)_Y$ symmetry, it does have a manifest $U(1)$ symmetry corresponding to a linear combination of generators:

$$Q = T_3 + \frac{Y}{2}\,, \tag{2.5}$$

where Q is the electromagnetic charge, Y is the hypercharge, and T_3 is the weak isospin. The fermions are then placed into left-handed iso-doublets and right-handed iso-singlets characterized by the quantum numbers T_3 and Y (see Table 2.2), where the left-handed and right-handed parts of a generic fermion field ψ are given by $\psi_{L,R} = 1/2(1 \mp \gamma^5)\psi$.

Families			T_3	Y	Q
$\begin{pmatrix} \nu_e \\ e \end{pmatrix}_L$	$\begin{pmatrix} \nu_\mu \\ \mu \end{pmatrix}_L$	$\begin{pmatrix} \nu_\tau \\ \tau \end{pmatrix}_L$	$1/2$	-1	0
			$-1/2$	-1	-1
ν_{eR}	$\nu_{\mu R}$	$\nu_{\tau R}$	0	0	0
e_R	μ_R	τ_R	0	-2	-1
$\begin{pmatrix} u \\ d \end{pmatrix}_L$	$\begin{pmatrix} c \\ s \end{pmatrix}_L$	$\begin{pmatrix} t \\ b \end{pmatrix}_L$	$1/2$	$1/3$	$2/3$
			$-1/2$	$1/3$	$-1/3$
u_R	c_R	t_R	0	$4/3$	$2/3$
d_R	s_R	b_R	0	$-2/3$	$-1/3$

Table 2.2: Fermion quantum numbers. The inclusion of right-handed neutrinos is speculative; they are not part of the Standard Model.

With these postulated representation assignments, the fermion Lagrangian can be written as

$$\mathcal{L}_{\text{Fermion}} = \sum_\psi \overline{\psi}\, i\gamma^\mu \partial_\mu\, \psi + J^\mu_{em}\, A_\mu + J^\mu_{NC}\, Z_\mu + J^{\pm\mu}_{CC}\, W^\pm_\mu\,, \tag{2.6}$$

where the fermionic currents that couple to the gauge-boson fields A, Z, and W are:

$$J^\mu_{em} = \sum_\psi Q_\psi\, \overline{\psi}\, \gamma^\mu \partial_\mu\, \psi\,, \tag{2.7}$$

$$J^\mu_{NC} = \frac{g}{2\cos\theta_{\text{W}}} \sum_\psi \overline{\psi}\, \gamma^\mu (g_V - g_A\gamma_5)\, \psi\,, \tag{2.8}$$

$$J^{\pm\mu}_{CC} = \frac{g}{\sqrt{2}} \sum_\psi \overline{\psi}_L\, \gamma^\mu T^\pm \psi_L\,, \tag{2.9}$$

respectively, and the sums of ψ run though all lepton and quark flavors. The familiar coupling constant of the electromagnetic interaction e is given by $e = g\sin\theta_{\text{W}}$, while the vector and axial-vector parts of the neutral weak current have the couplings $g_V = T_3 - 2\,Q\sin^2\theta_{\text{W}}$ and $g_A = T_3$. It is interesting to note that the weak force does not conserve parity — the W boson interacts only with the left-handed particles (or right-handed antiparticles).

The Yang-Mills Lagrangian can then be written in terms of the field strength

tensors as

$$\mathcal{L}_{\text{Yang-Mills}} = -\frac{1}{4}B^{\mu\nu}B_{\mu\nu} - \frac{1}{4}W_i^{\mu\nu}W^i_{\mu\nu}\,, \tag{2.10}$$

predicting triple and quartic boson couplings. The couplings between the neutral bosons are forbidden and the only allowed triple and quartic boson vertices require at least two charged bosons.

The Higgs Mechanism

The Higgs boson is a spin-0 particle which breaks the $SU(2)_L \times U(1)_Y$ symmetry of the Standard Model by acquiring a vacuum expectation value. The Higgs field is chosen to be a complex doublet, which is the simplest possible non-trivial representation of $SU(2) \times U(1)$, and the Higgs Lagrangian has the form:

$$\mathcal{L}_{\text{Higgs}} = (\mathcal{D}^\mu\Phi)^\dagger(\mathcal{D}_\mu\Phi) - V(\Phi^\dagger\Phi)\,, \tag{2.11}$$

where the potential function V is the $SU(2)_L$ invariant potential of the Higgs field:

$$V(\Phi^\dagger\Phi) = \mu^2\Phi^\dagger\Phi + \lambda(\Phi^\dagger\Phi)^2. \tag{2.12}$$

The potential must increase with $(\Phi^\dagger\Phi)$, hence $\lambda > 0$, while the mass parameter μ^2 can still be negative. In this case the potential has a non-trivial minimum value V_{min} for

$$\Phi^\dagger\Phi = -\frac{\mu^2}{2\lambda} \equiv \frac{v^2}{2} > 0\,, \tag{2.13}$$

where $v/\sqrt{2}$ is the vacuum expectation value of the Higgs field. The $SU(2)_L$ symmetry of the Higgs potential leads to a whole family of Higgs ground states. After choosing a specific one as the vacuum ground state, a gauge rotation allows us to write its expansion as

$$\Phi(x) = \frac{1}{\sqrt{2}}\begin{pmatrix} 0 \\ v + H(x) \end{pmatrix}, \tag{2.14}$$

leaving only one physical Higgs boson $H(x)$. This vacuum expectation breaks the $SU(2) \times U(1)$ symmetry and results in a Lagrangian describing not only a massive Higgs boson but also massive vector fields W and Z:

$$\mathcal{L}_{\text{Higgs}} = \frac{1}{2}\Big[\frac{(g'^2+g^2)\,v^2}{4} Z_\mu Z^\mu + \frac{g^2 v^2}{4}(W_\mu^+ W^{-\mu} + W_\mu^- W^{+\mu}) + (2\mu^2 H^2)\Big] + ... \quad (2.15)$$

It should be noted that the photon field A remains massless. The boson masses are then given by

$$\begin{aligned} M_Z &= \frac{\sqrt{g'^2+g^2}\,v}{2}\,, \\ M_W &= \frac{gv}{2}\,, \\ M_\gamma &= 0\,, \\ M_H &= \sqrt{2}\mu\,. \end{aligned} \quad (2.16)$$

Mass terms for the fermions are introduced via Yukawa couplings of the fermion fields to the doublet Higgs field, and the Yukawa Lagrangian can written as

$$\mathcal{L}_{\text{Yukawa}} = -\frac{v+H}{\sqrt{2}} g_f \bar{f} f\,, \quad (2.17)$$

which immediately gives the fermion masses as $m_f = v g_f/\sqrt{2}$. The remaining Lagrangian terms proportional to H describe the fermion-Higgs interactions with a coupling strength m_f/v. The fermion masses differ by several orders of magnitude (see Table 2.1) and the Standard Model contains no explanation for this effect.

2.1.3 Status of the Standard Model

The Standard Model has had tremendous success in describing the considerable amount of data from all high-energy collider experiments. The LEP Electroweak Working Group combines the most important measurements from the LEP, Tevatron and SLD experiments in a single fit to the Standard Model [10]. Figure 2.2 shows the pull distribution for 18 measurements used in this fit, including the direct measurements of the top quark mass and the masses and widths of the W and Z bosons. For

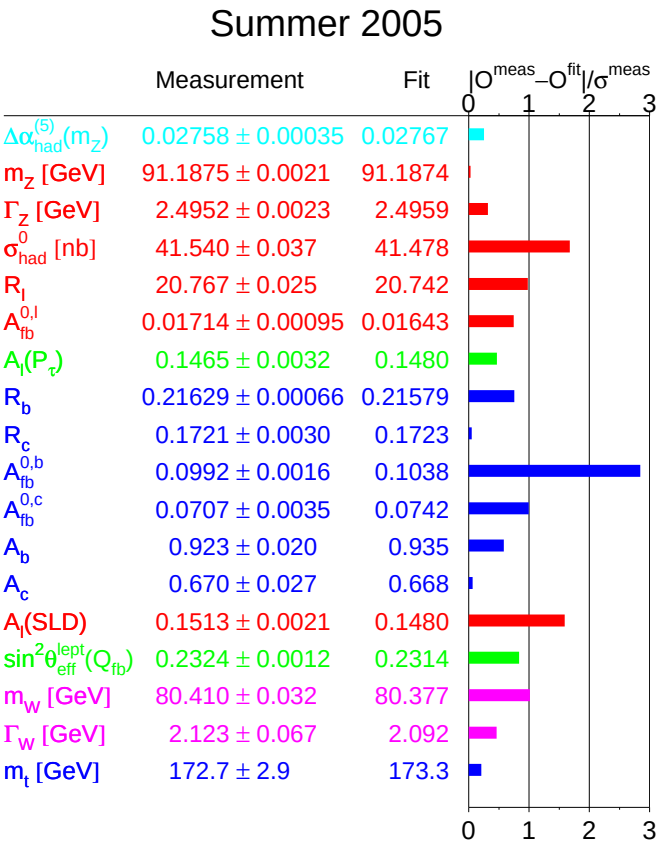

Figure 2.2: Precision electroweak measurements and their pulls, derived from the global fit to the Standard Model (as of Summer 2005).

a given parameter, the pull is defined as the difference between the measured value of this parameter and the best-fit divided by the measurement error (standard deviation). A very good agreement between the fitted and measured parameter values is observed.

The precision measurements of the electroweak parameters depend logarithmically on the Higgs boson mass through radiative corrections. Therefore, the global fit can be used to constrain the Higgs mass in the Standard Model. Figure 2.3 shows the $\Delta\chi^2$ of the fit, which gives the preferred value of the Higgs mass as

$$M_H = 91^{+45}_{-32}\ \text{GeV}, \tag{2.18}$$

which in turn can be translated into an upper limit of $M_H < 186$ GeV at the 95% con-

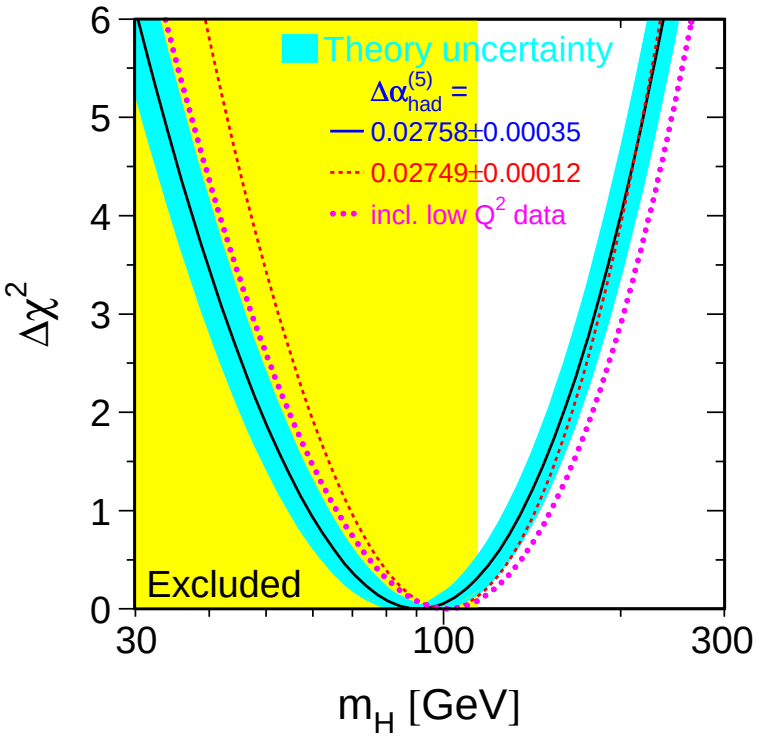

Figure 2.3: $\Delta\chi^2$ of the global fit to the precision electroweak data as a function of the Higgs boson mass (as of Summer 2005). The shaded region on the left corresponds to the limit on the Higgs mass from the direct searches at LEP2.

fidence level [10]. It should be noted that direct searches for Higgs production at LEP lead to the conclusion that the Standard-Model Higgs should be heavier than 114.4 GeV (95% confidence level) [11]. The Higgs discovery is the main goal of the upcoming Large Hadron Collider (LHC) physics program, and the above limits indicate that the Standard Model Higgs is well within the reach of the LHC.

Despite its apparent success, the Standard Model raises many unanswered questions, e.g., it does not explain the large differences in particle masses, why there are three fermion generations, what is the source of CP violation, or how to solve the hierarchy problem of the Higgs mass.

Eventually one would also like to include gravity in a unified theory along with other particle interactions. This brings up another question: why the Planck scale ($M_{\rm Pl} \sim 10^{19}$ GeV) is so much bigger than the electroweak scale ($M_{\rm EW} \sim 10^2$ GeV).

These and other inherent problems of the Standard Model cannot be solved without the introduction of some *new physics* [12]. Two of the most popular extensions of the Standard Model, supersymmetry and models with large extra dimensions, are discussed in the next chapter.

Recently the first clear sign of physics beyond the Standard Model has been found in the form of neutrino oscillations. Experiments using neutrinos generated by cosmic-ray interactions in the atmosphere, by nuclear fusion in the Sun, and by nuclear fission in reactors have established neutrino-flavor oscillations: $\nu_\mu \to \nu_\tau$ and $\nu_e \to \nu_\mu/\nu_\tau$ [13]. As a consequence, the neutrinos should have non-zero masses, which violates one of the Standard Model assumptions. Combining the neutrino oscillation data with direct limits on the neutrino masses (see Table 2.1) yields masses in the sub-eV range [14]. This should not have any noticeable impact on the physics results in this thesis where the neutrinos are assumed to be massless, as expected in the Standard Model.

2.2 Neutrino Production at LEP

Neutrino pair-production accompanied by one or more photons is the only irreducible background for new physics processes involving photons and missing energy in the final state. On the other hand, a study of this process is interesting in itself since it allows one to verify the predictions of the Standard Model and determine the number of light neutrino species. A deviation from the Standard Model value of $N_\nu = 3$ would constitute a clear indication of new physics, e.g., it would suggest the existence of a new fermion generation.

In the Standard Model reaction $e^+e^- \to \nu\bar{\nu}\gamma(\gamma)$, the photons are radiated mainly from the incoming electrons and positrons, a process called *initial-state radiation* (ISR or *bremsstrahlung*).[1] Therefore a precise measurement of this process provides a unique opportunity to test and improve the present understanding of the ISR and other higher-order QED effects in the fermion and boson production in high-energy

[1] Final-state radiation is not allowed because the neutrinos are neutral particles. However, for a small fraction of events, the photon is radiated from the internal W boson propagator.

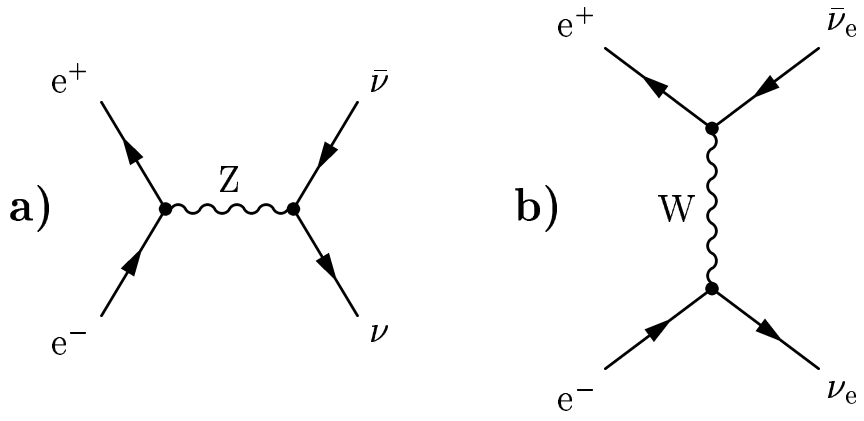

Figure 2.4: Feynman diagrams of the tree-level process $e^+e^- \to \nu\bar{\nu}$. In the s–channel, all three neutrino species are pair-produced via Z exchange a), whereas only electron neutrinos are allowed in the t–channel W exchange b).

e^+e^- collisions. An accurate description of such corrections is required for the precision measurements at LEP[2] and at future high-energy e^+e^- colliders.

2.2.1 The Reaction $e^+e^- \to \nu\bar{\nu}$

In the Standard Model, the reaction $e^+e^- \to \nu_l\bar{\nu}_l$ proceeds through s–channel Z exchange for all three neutrino flavors ($\nu_l = \nu_e, \nu_\mu, \nu_\tau$) and through t–channel W exchange for electron neutrinos only. The lowest order (*Born Approximation*) diagrams of this process are shown in Figure 2.4. Using the Feynman rules, the amplitudes $\mathcal{M}_Z$ and $\mathcal{M}_W$ corresponding to these diagrams can be written as

$$\begin{aligned} \mathcal{M}_{\mathcal{Z}} &= \sum_{l=e,\mu,\tau} \frac{g^2}{2\cos^2\theta_W}(\bar{\nu}_l\gamma_\mu P_L\nu_l)\frac{g^{\mu\sigma} - q_Z^\mu q_Z^\sigma/M_Z^2}{M_Z^2 - q_Z^2}\left[\, g_R\bar{e}\gamma_\sigma P_R e + g_L\bar{e}\gamma_\sigma P_L e\,\right], \\ \mathcal{M}_{\mathcal{W}} &= \frac{g^2}{2}(\bar{e}\gamma_\mu P_L\nu_e)\frac{g^{\mu\sigma} - q_W^\mu q_W^\sigma/M_W^2}{M_W^2 - q_W^2}(\bar{\nu}_e\gamma_\sigma P_L e)\,, \end{aligned} \tag{2.19}$$

where $P_{L,R} = (1 \mp \gamma^5)/2$ denotes the chiral projection operators and $g_R \equiv (g_V - g_A)/2 = \sin^2\theta_W$ and $g_L \equiv (g_V + g_A)/2 = -\frac{1}{2} + \sin^2\theta_W$ are the coupling constants of the right- and left-handed electrons to the Z boson.

[2]For example, the uncertainty on the theoretical description of the initial- and final-state radiation in the reaction $e^+e^- \to W^+W^- \to 4f(\gamma)$ is an important source of systematic errors on the measurement of the W boson mass at LEP [15].

The Born-level cross section is then given by [16]

$$\sigma^0_{e^+e^-\to\nu\bar{\nu}}(s) = \frac{N_\nu G_F^2}{6\pi} M_Z^4 (g_R^2 + g_L^2) \frac{s}{[(s-M_Z^2)^2 + (M_Z\Gamma_Z)^2]}$$
$$- \frac{G_F^2}{\pi} g_L \frac{M_W^2 M_Z^2 (s-M_Z^2)}{(s-M_Z^2)^2 + (M_Z\Gamma_Z)^2} \left[\frac{(s+M_W^2)^2}{s^2} \log\left(\frac{s+M_W^2}{M_W^2}\right) - \frac{M_W^2}{s} - \frac{3}{2} \right]$$
$$+ \frac{G_F^2}{\pi} M_W^2 \left[\frac{s+2M_W^2}{2s} - \frac{M_W^2}{s} \left(\frac{s+M_W^2}{s}\right) \log\left(\frac{s+M_W^2}{M_W^2}\right) \right], \qquad (2.20)$$

where $\sqrt{s}$ is the center-of-mass energy, Γ_Z is the width of the Z boson, and G_F is the Fermi coupling constant ($G_F/\sqrt{2} = g^2/8M_W^2$). The three terms in Equation 2.20 originate from the square of the Z−amplitude, the W−Z interference, and the square of the W−amplitude, respectively. The first term is the only one sensitive to the number of light neutrino species N_ν since only the electron neutrinos can be produced in the t–channel. It should be noted that in the Standard Model, the cross sections of the $\nu_\mu\bar{\nu}_\mu$ and $\nu_\tau\bar{\nu}_\tau$ pair-production can be assumed to be identical since small effects arising from possibly nonzero neutrino masses are undetectable at LEP.

The Born-level cross section of the reaction $e^+e^-\to\nu\bar{\nu}$ is shown in Figure 2.5a.[3] At energies around the Z pole, $\sqrt{s} \simeq 91$ GeV (LEP1 energy range), the $\nu_e\bar{\nu}_e$ and $\nu_\mu\bar{\nu}_\mu$ cross sections are almost the same reaching the maximum value of 3.9 nb, and the t–channel contribution to the $\nu_e\bar{\nu}_e$ cross section amounts to only about 1%. The situation changes at LEP2 energies, $\sqrt{s} \simeq 200$ GeV, where the t–channel contribution clearly dominates, $\sigma_{Born}(\nu_e\bar{\nu}_e) = 40$ pb and $\sigma_{Born}(\nu_\mu\bar{\nu}_\mu) = 1$ pb.

The inclusion of the ISR and other higher-order QED corrections is very important for this process. Figure 2.5b shows the cross section of the reaction $e^+e^-\to\nu\bar{\nu}(\gamma)$,[4] as predicted by the `KKMC` program [17] which takes into account the ISR effects (see Section 2.2.3). Comparing the ISR-corrected and Born-level cross sections, we can see that at LEP2 the inclusion of ISR increases the total $\nu_\mu\bar{\nu}_\mu(\gamma)$ cross section by a factor of seven, $\sigma_{ISR}(\nu_\mu\bar{\nu}_\mu) \simeq 7$ pb. This effect can be easily understood by examin-

[3] Here and in the following, the index l for the different neutrino species is omitted and a sum of all generations is denoted as "$\nu\bar{\nu}$."

[4] The "(γ)" in the formula indicates the possible emission of one or more photons.

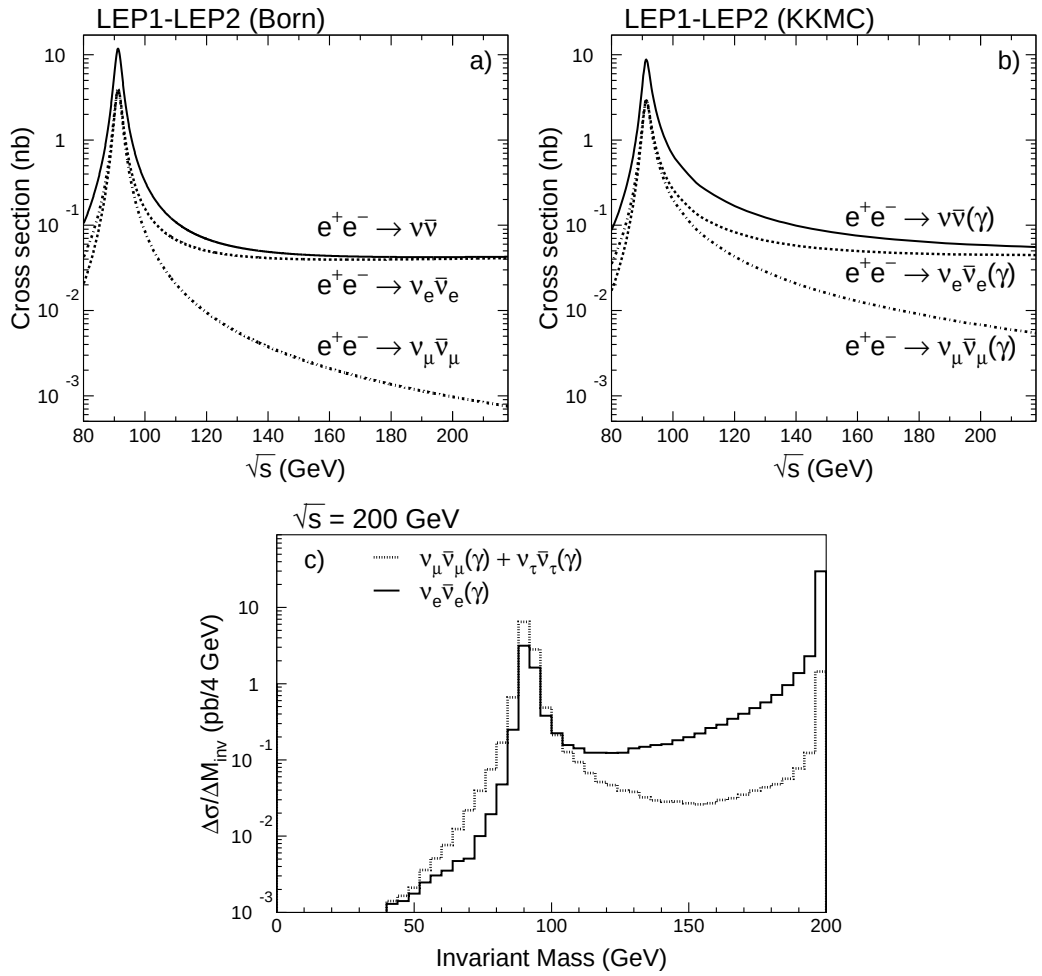

Figure 2.5: Total cross section of the reaction $e^+e^- \to \nu\bar{\nu}(\gamma)$ as a function of the center-of-mass energy a) at Born-level and b) as predicted by the KKMC program. c) The $\nu\bar{\nu}$ invariant mass distribution at $\sqrt{s} = 200$ GeV for an event sample generated with the KKMC program. Contributions from different neutrino species are shown separately.

ing the invariant mass distribution of the $\nu\bar{\nu}$ pairs (see Figure 2.5c). For the muon neutrinos, the majority of generated events have the invariant mass close to the Z mass: $M_{inv}(\nu_\mu\bar{\nu}_\mu) \simeq M_Z$. Thus, the photon emission has the effect of reducing the effective center-of-mass energy from 200 GeV to about 91 GeV, where the Born-level cross section is much higher. The Z bosons in the s–channel are produced predominantly on-shell. This effect, called *the radiative return to the Z*, was observed for all fermion pair-production processes at LEP2. The resulting peak in the two-fermion invariant mass distribution is often referred to as *the Z-return peak*. Figure 2.5c also

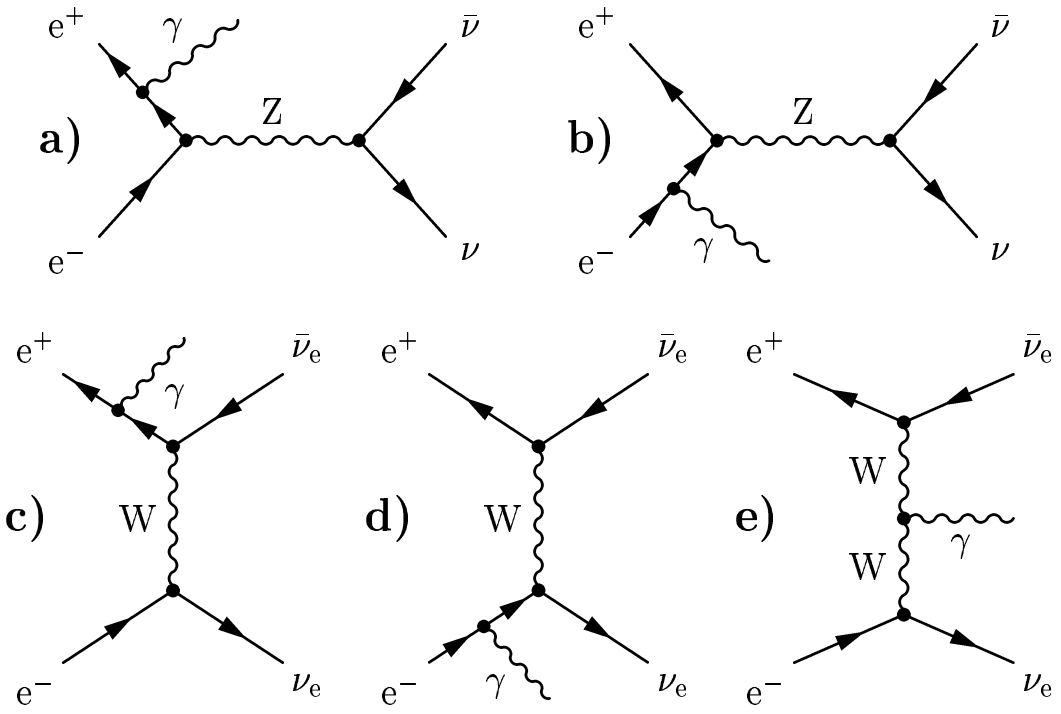

Figure 2.6: Lowest-order Feynman diagrams for the reaction $e^+e^- \to \nu\bar{\nu}\gamma$.

shows that the electron neutrinos are produced predominantly in the t–channel, where $M_{inv}(\nu_e\bar{\nu}_e) \simeq \sqrt{s}$.

2.2.2 Production of Single- and Multi-Photon Events at LEP

As shown in Figure 2.6, the reaction $e^+e^- \to \nu\bar{\nu}\gamma$ proceeds mainly via initial state radiation from the incoming electrons and positrons. In addition, a small fraction of photons ($\simeq 0.5\%$) can be emitted in the t–channel W boson fusion (Figure 2.6e) [18]. Since the produced neutrinos are undetectable,[5] such events would lead to the single-photon and missing energy signature. Therefore, the total rate of the initial state radiation as well as the energy and angular distributions of the emitted photons have to be known to a high precision.

A general and simple approach to this problem is to "dress" the Born-level cross

[5]Only a tiny fraction ($\sim 10^{-9}$) of 100 GeV neutrinos would interact with the material of the L3 detector [19].

section of the $\nu\bar{\nu}$ pair production ($\sigma_0(s)$) with a radiator function $H(x_\gamma, \theta_\gamma; s)$ [20]:

$$H = \frac{\alpha}{2\pi}\frac{1}{x_\gamma}\left[2\,\frac{1+(1-x_\gamma)^2}{\sin^2\theta_\gamma + 4m_e^2/s} - x_\gamma^2\right], \tag{2.21}$$

where $x_\gamma = E_\gamma/E_{beam}$, m_e is the electron mass, and α is the QED coupling constant. The differential cross section of the reaction $e^+e^- \to \nu\bar{\nu}\gamma$ can then be evaluated as

$$\frac{d\sigma}{dx_\gamma d\cos\theta_\gamma} = \sigma_0([1 - x_\gamma]\cdot s)\cdot H(x_\gamma, \theta_\gamma; s)\,. \tag{2.22}$$

Examining Equation 2.21, we can see that the differential cross section is expected to peak at low photon energies and polar angles. In addition, Equation 2.22 explains the appearance of the Z-return peak. In the s–channel, the Born-level cross section $\sigma_0(s)$ is very high near the Z pole so that the differential cross section has a maximum for photons with *recoil mass* close to the Z boson mass. The photon recoil mass is defined as the invariant mass recoiling against the photon(s) and is given by

$$M_{\rm rec} \;=\; \sqrt{\left(\sqrt{s} - E_\gamma\right)^2 - |\vec{p}_\gamma|^2}\,, \tag{2.23}$$

where $E_\gamma = \sum_i E_{\gamma_i}$ and $\vec{p}_\gamma = \sum_i \vec{p}_{\gamma_i}$ are the total energy and momentum of the photons. For single-photon events, Equation 2.23 simplifies to $M_{\rm rec} = \sqrt{s - 2\sqrt{s}E_\gamma}$. The position of the Z-return peak in the recoil mass distribution is independent of the collision energy. Therefore, instead of using the photon energy variable, the photon recoil mass is usually used.

The radiator function approach is capable of calculating the total cross section of the single-photon production with a precision of about 4% [21]. This level of accuracy is not satisfactory for my analysis. Therefore, I use specially developed Monte Carlo programs to simulate the $e^+e^- \to \nu\bar{\nu}\gamma(\gamma)$ process (see next section). The following differential distributions were obtained using the `KKMC` program.

As discussed in Chapter 6, the main variables used in the selection of single- and multi-photon events were the photon polar angle (θ_γ) and transverse momentum, $P_t^\gamma = E_\gamma \sin\theta_\gamma$. Because the efficiency of the L3 tracker decreased rapidly with polar

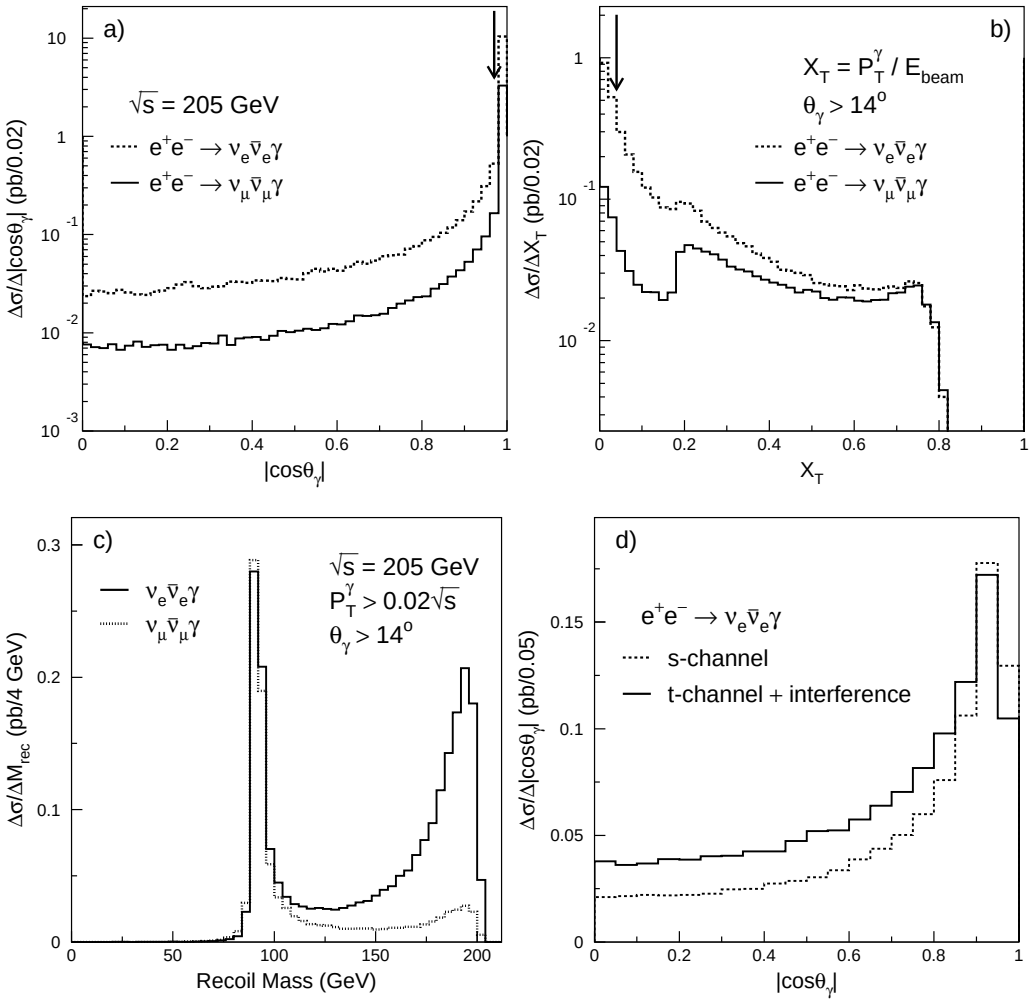

Figure 2.7: Distributions of a) the polar angle and b) the transverse momentum for single-photon events generated with a threshold $E_\gamma > 1$ GeV, at $\sqrt{s} = 205$ GeV. The arrows indicate the "selection" cuts. Distributions of c) the recoil mass and d) the polar angle after the application of these cuts.

angle, a lower cut on the polar angle of the photon had to be applied[6] $14^\circ < \theta_\gamma < 166^\circ$. The main background to this topology stemmed from the radiative Bhabha scattering process, $e^+e^- \to e^+e^-\gamma$, where both electrons were lost in the beam pipe, and only a photon was scattered at a large polar angle. To reject such events, the transverse momentum of the photon was required to be above $0.02\sqrt{s}$. These two "selection" cuts defined the phase space region of my single-photon selection.

As shown in Figure 2.7a, the angular cut rejected about 80% of both the $\nu_\mu\bar{\nu}_\mu\gamma$ and $\nu_e\bar{\nu}_e\gamma$ events. The distribution of the scaled transverse momentum, $x_t = P_t^\gamma / E_{beam}$,

[6]The BGO electromagnetic calorimeter of L3 extended down to $\theta_{min}(\mathrm{BGO}) = 10^\circ$.

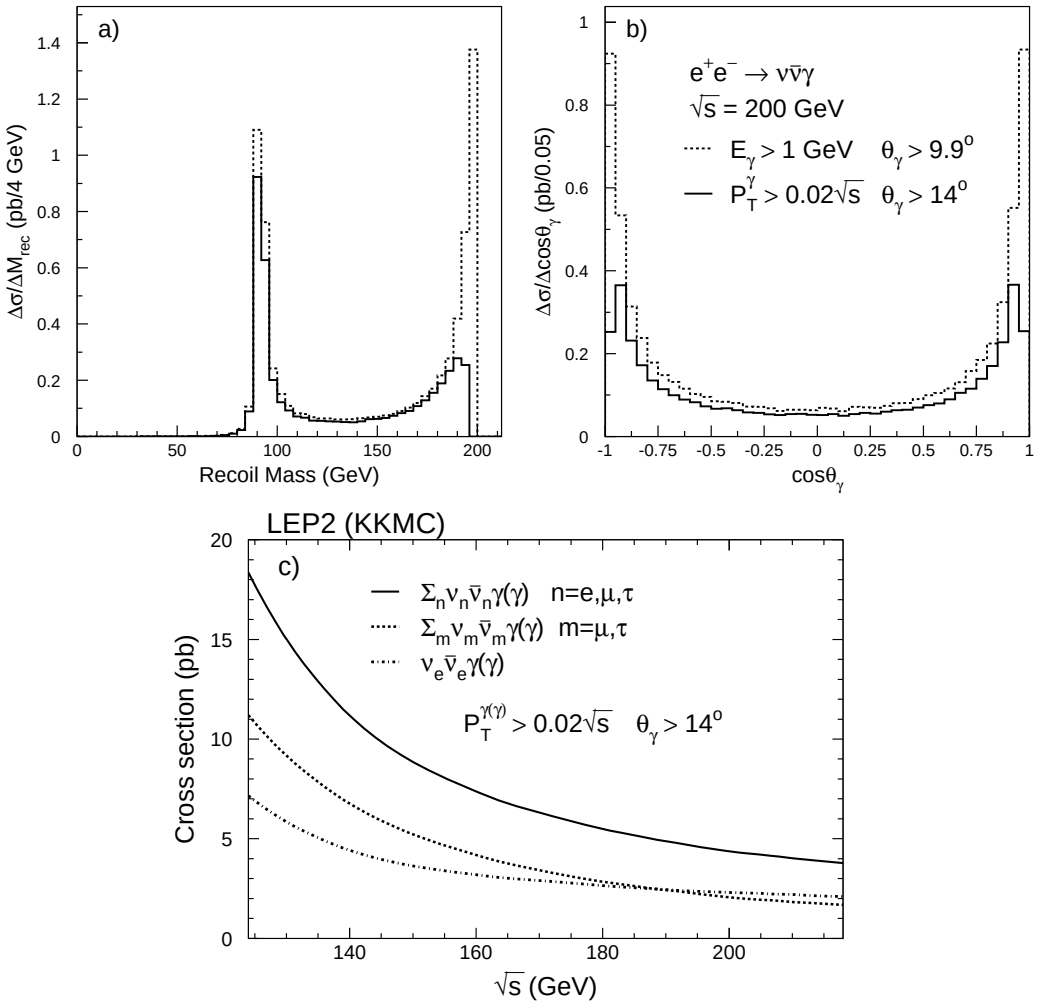

Figure 2.8: Differential cross sections of the reaction $e^+e^- \to \nu\bar{\nu}\gamma$ as functions of a) the recoil mass and b) $\cos\theta_\gamma$, calculated with the KKMC program at $\sqrt{s} = 200$ GeV. c) Total cross section of the reaction $e^+e^- \to \nu\bar{\nu}\gamma(\gamma)$.

after this cut is shown in Figure 2.7b. The visible peak structure at $x_t \simeq 0.02$ comes from the events in the Z-return peak. The cut on the transverse momentum, $P_t^\gamma > 0.02\sqrt{s}$, rejected only about 15% of the $\nu_\mu\bar{\nu}_\mu\gamma$ events and about 40% of the $\nu_e\bar{\nu}_e\gamma$ events.

Figures 2.7c,d show the recoil mass and polar angle distributions of the single-photon events passing these "selection" cuts. While the Z-return peak is present in both the electron- and muon-neutrino radiative spectra, the $\nu_e\bar{\nu}_e\gamma$ production dominates in the region of high recoil masses (low photon energies).

Since the neutrinos escaped detection, one could not distinguish between the $\nu_e\bar{\nu}_e\gamma$

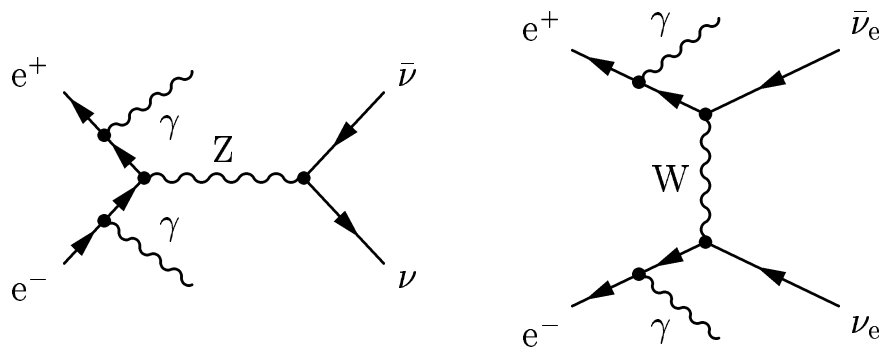

Figure 2.9: Lowest-order Feynman diagrams for the reaction $e^+e^- \to \nu\bar{\nu}\gamma\gamma$. Only two of the 19 allowed diagrams are shown.

and $\nu_\mu\bar{\nu}_\mu\gamma$ final states. The combined $\nu\bar{\nu}\gamma$ distributions of the photon recoil mass and polar angle are shown in Figures 2.8a,b. For comparison, these figures also show the same distributions obtained after relaxing the "selection" cuts to $E_\gamma > 1$ GeV and $\theta_\gamma > \theta_{min}(\mathrm{BGO}) = 10°$, which roughly corresponds to the energy and angular acceptance of the BGO electromagnetic calorimeter (see Chapters 4 and 5).

The total cross section of the single- and multi-photon production processes is shown in Figure 2.8c, where events with more than one photon with $E_\gamma > 1$ GeV and $\theta_\gamma(180° - \theta_\gamma) > 14°$ are also included. This plot shows that at LEP2 ($\sqrt{s} \simeq 200$ GeV) the radiative production of the electron neutrinos was as large as the combined production of the muon and tau neutrinos, $\sigma(\nu_e\bar{\nu}_e\gamma(\gamma)) \simeq \sigma(\nu_\mu\bar{\nu}_\mu\gamma(\gamma)) + \sigma(\nu_\tau\bar{\nu}_\tau\gamma(\gamma))$.

Multi-Photon Production in the Standard Model

As will be discussed in the next chapter, several supersymmetric processes can lead to the *multi-photon and missing energy* final state via $e^+e^- \to YY \to XX\gamma\gamma$, where X and Y are new neutral invisible particles. Therefore, it is interesting to consider the production of multi-photon events in the Standard Model, $e^+e^- \to \nu\bar{\nu}\gamma\gamma(\gamma)$.

This process corresponds to a total of 6 Feynman diagrams for the $\nu_\mu\bar{\nu}_\mu\gamma\gamma$ production and 19 Feynman diagrams for the $\nu_e\bar{\nu}_e\gamma\gamma$ production. These diagrams correspond to all possible combinations of two photons emitted from the incoming electron and positron as well as from the W boson propagator in the t–channel. As an example, two of such Feynman diagrams are shown in Figure 2.9.

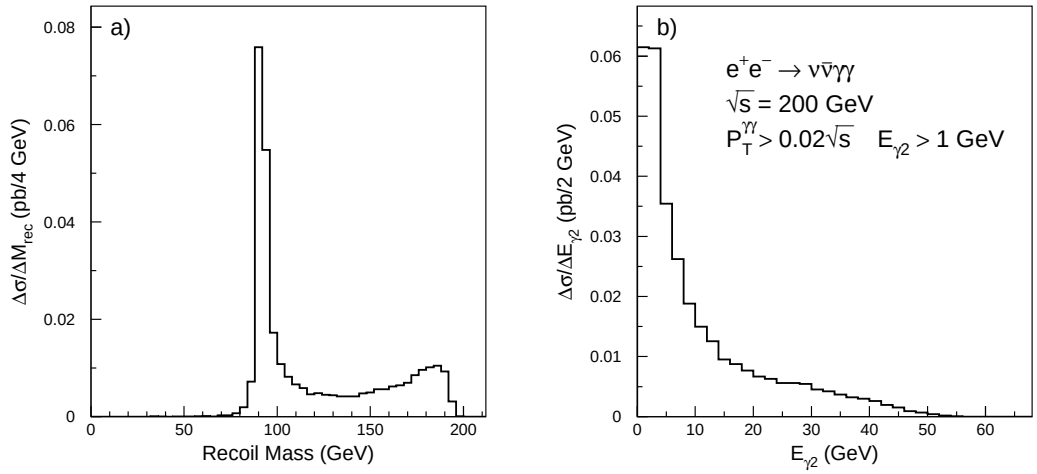

Figure 2.10: Differential cross sections of the $e^+e^- \to \nu\bar{\nu}\gamma\gamma$ process as functions of a) the recoil mass and b) the energy of the second photon, calculated with the KKMC program at $\sqrt{s} = 200$ GeV.

A multi-photon and missing energy event is defined as having at least two photons with $E_\gamma > 1$ GeV and $\theta_\gamma(180^\circ - \theta_\gamma) > 14^\circ$. In addition, the transverse momentum of the multi-photon system should satisfy $P_t^{\gamma\gamma} > 0.02\sqrt{s}$. Figure 2.10 shows the differential cross sections of this reaction as functions of the recoil mass and the energy of the second most energetic photon (E_{γ_2}). While the recoil mass distribution has the familiar feature of the Z-return peak, the E_{γ_2} spectrum is dominated by soft photons, exhibiting the behavior expected from Equations 2.21 and 2.22. At LEP2, the total cross section of the $e^+e^- \to \nu\bar{\nu}\gamma\gamma$ process was about 15 times smaller than that of the $e^+e^- \to \nu\bar{\nu}\gamma$ process.

2.2.3 Monte Carlo Event Generators

In order to estimate the efficiency of the $e^+e^- \to \nu\bar{\nu}\gamma(\gamma)$ event reconstruction and selection, I rely on Monte Carlo (MC) simulations. I also use MC programs to calculate the expected rate of the single- and multi-photon production in the Standard Model and to estimate systematic errors caused by uncertainties in the theoretical modelling of these processes.

During the final years of the LEP2 program, from 1998 to 2000, the four LEP experiments collected about 2.5 fb^{-1} of data at $\sqrt{s} = 189 - 208$ GeV. The statistical

error of the corresponding $\nu\bar{\nu}\gamma(\gamma)$ cross section measurement is expected to be below 2%. Thus, the expected cross section have to be known with a relative precision of at least 1%, and the corresponding differential distributions have to be simulated with a similar level of accuracy.

Up to the year 2000, most of the LEP experiments had used the `KORALZ` MC event generator [22]. It was originally written to simulate the $\tau\bar{\tau}$ pair-production and decay at energies near the Z pole (LEP1) and was later extended to include the $\nu\bar{\nu}\gamma(\gamma)$ process. The `KORALZ` generator did not use the exact cross section of the tree-level reaction $e^+e^- \to \nu\bar{\nu}\gamma$ so that contributions from the t–channel W exchange diagrams were added using rather simple approximations [23]. This resulted in a systematic uncertainty of about 4% on the single-photon cross section, while for the multi-photon final states the systematic uncertainty could be as high as 10% [24].

In 2000, the `KORALZ` event generator was replaced by a more advanced and precise MC program, `KKMC` [17]. Initially, it could be used to simulate any fermion pair-production processes, $e^+e^- \to f\bar{f}(\gamma)$, except for Bhabha scattering and neutrino pair-production. The $\nu\bar{\nu}\gamma(\gamma)$ production process was later incorporated in this program and a further-improved version was released in September 2002 as `KKMC v4.19`. This version of the `KKMC` generator was the main source of single- and multi-photon Monte Carlo events for my analyses.

The `KKMC` program includes the complete $\mathcal{O}(\alpha^2)$ calculations for the reaction $e^+e^- \to \nu\bar{\nu}\, n\gamma$ with $n = 1, 2$, including contributions from diagrams with the emission of one real and one virtual photon. The higher-order ISR and other QED corrections are calculated using the YFS-inspired Coherent Exclusive Exponentiation scheme [25], as discussed in Section A.3. The complete $\mathcal{O}(\alpha)$ electroweak corrections with higher-order extensions are implemented using the `DIZET` library [26].

The systematic errors are estimated to be about 0.8%, 1.3%, and 5% for the $\nu_\mu\bar{\nu}_\mu\gamma$, $\nu_e\bar{\nu}_e\gamma$, and $\nu\bar{\nu}\gamma\gamma$ production processes, respectively [24]. Thus, the `KKMC` program achieved the goal of a one percent precision on the total cross section of the $e^+e^- \to \nu\bar{\nu}\gamma(\gamma)$ process.

An independent cross check is provided by the `NUNUGPV` event generator [27]. It

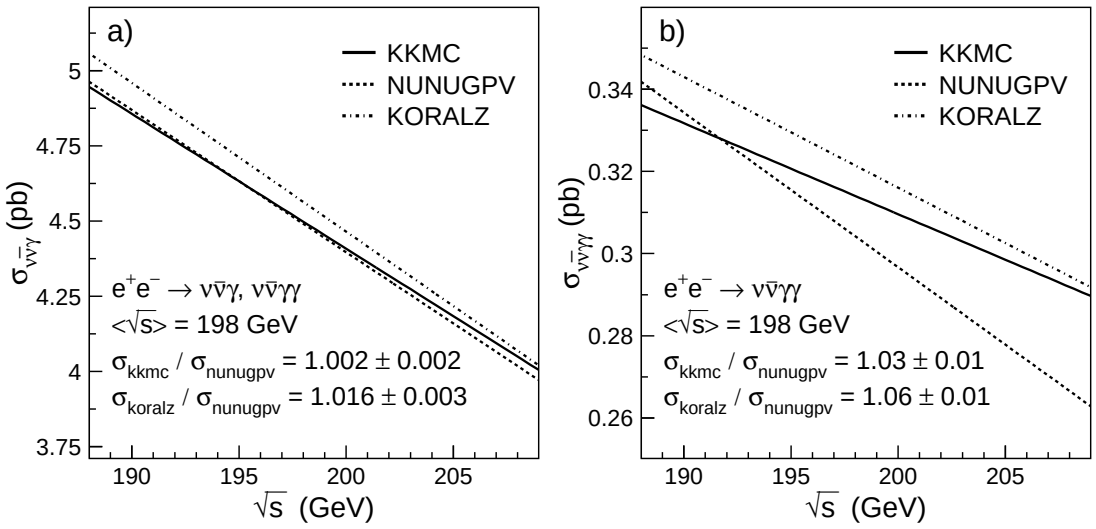

Figure 2.11: Total cross sections a) of the combined single- and multi-photon production process and b) of the multi-photon production process, as predicted by the KKMC, NUNUGPV, and KORALZ event generators.

includes the exact matrix elements for the reactions $e^+e^- \to \nu\bar{\nu}\, n\gamma$, with $n = 1, 2, 3$. The ISR and other higher-order QED corrections are calculated using the Structure Function techniques (see Section A.2). The main limitation of the NUNUGPV program is the absence of the exact $\mathcal{O}(\alpha)$ electroweak corrections, which results in a precision of 1–2% for the simulation of the single-photon production process [28]. In addition, contrary to the KKMC generator, the NUNUGPV program cannot be used for the inclusive reaction $e^+e^- \to \nu\bar{\nu}(\gamma)$. The main advantage of the NUNUGPV is its ability to simulate the single- and multi-photon production processes in the presence of anomalous triple and quartic gauge-boson couplings. Therefore, I will use this program in my search for anomalous boson couplings.

Figure 2.11 shows a comparison between the KKMC, NUNUGPV, and KORALZ event generators in the energy range studied in this thesis, $\sqrt{s} = 189 - 208$ GeV. The cross section curves predicted by the KKMC and NUNUGPV show an excellent agreement, well within the expected theoretical precision. A clear improvement over the accuracy level of the KORALZ is also observed.

The specific algorithms used in the KKMC and NUNUGPV Monte Carlo programs are described in more detail in Appendix A.